5 Dynamic Stall and its Associated Wake

In this chapter an examination of the wake structure for various reduced frequencies ($0.05 < k < 0.3$) has been performed for a pure-plunging and analogous pure-pitching airfoil. Combined motions of pitching and plunging are then examined using direct-force measurements, specifically to determine the level of hysteresis and potential augmentation in lift attainable through dynamic stall.

5.1 Parameter Space

Sinusoidal movements based on the following equations for pitch (α) and plunge (h) have been tested at large plunge amplitudes of $h_o = 0.5c$ and frequencies up to $f = 3$Hz; note for all investigations the pitch motion lead the plunge motion by $\phi = 90°$:

$$\alpha(t) = \alpha_o + \alpha_1 \cos(2\pi f t + \phi), \tag{5.1}$$

$$h(t) = h_o \cos(2\pi f t). \tag{5.2}$$

The effective angle of attack was defined in the following manner:

$$\alpha_{eff}(t) = \alpha_o + \alpha_1 \cos(2\pi f t + \phi) + \dot{h}/U_\infty + c\dot{\alpha}/2U_\infty, \tag{5.3}$$

whereby the last term, often referred to as *dynamic cambering*, was neglected since its contribution was found to be minimal at these reduced frequencies. When comparing pure-pitch versus pure-plunge motions a maximum phase advance of $t/T = 0.04$ in the effective angle-of-attack distribution for the pure-pitch case was observed for the most extreme case at $k = 0.25$. This discrepancy fell within the experimental error and therefore was ignored.

Varied were the angle-of-attack mean (α_o) and amplitude (α_1) values, but always with asymmetric incidences since the objective of the study was to look for lift augmentation through the dynamic-stall process. Also varied was the reduced frequency (k), which was based on the airfoil chord length. The range of reduced frequencies examined in this study represents forward flight for most birds, bats and large insects ($0.05 < k < 0.3$). The following table outlines the combined-motion (pitching and plunging) cases examined in this study:

Table 5.1: Description of combined pitching and plunging cases tested.

k	α_o	α_1
0.05	5°, 10°	0°, -5°, -10°
0.1	5°, 10°	2.5°, -2.5°, -7.5°

5.2 Results

5.2.1 Effect of Reduced Frequency

To at first qualitatively investigate the nature of the dynamic-stall phenomenon and its associated wake, smoke-visualization studies were performed for various pure-plunging

cases and for a range of reduced frequencies ($0.05 < k < 0.3$). These studies elucidated the importance of the reduced frequency on the character of the wake. At lower reduced frequencies ($k < 0.15$) it was found that the dynamic-stall process and its associated shedding corresponded to a typical bluff-body-type von Kàrman street with multiple alternating vortices shed from the leading and trailing edges. Up to four sets of such vortex pairs were shed over the downstroke. For higher reduced frequencies ($k > 0.2$) where the kinematic forcing was much more dominant, a single leading-edge and trailing-edge vortex pair was shed into the wake forming a so-called *mushroom*-wake structure as described by Panda and Zaman (1994). A qualitative sketch of these general differences in the wake is depicted in Fig. 5.1.

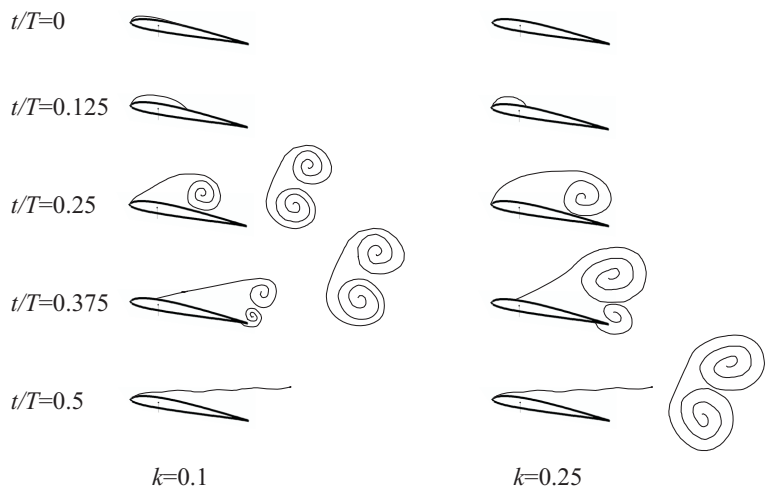

Figure 5.1: Comparison of the wake formation during the downstroke for pure-plunging motions at two reduced frequencies with $\alpha_o = 8°$; note at the higher reduced frequency a single yet more distinct vortex pair known as a *mushroom* structure is shed into the wake.

5.2.2 Pure-Pitch versus Pure-Plunge Decomposition

The relative positioning of the shed vortices in the wake with respect to the airfoil is crucial to the lift and moment production in that each shed vortex influences the strength of the bound vortex. This interaction is often referred to as the circulatory contribution. This vortex positioning has been further examined by comparing two equivalent cases (pure-plunging versus pure-pitching). This comparison was made at two reduced frequencies, the first representative of bluff-body-type shedding ($k = 0.1$) and the second of mushroom-wake-type shedding ($k = 0.25$). For the bluff-body-type case, both lift and moment measurements were performed. It can be seen in Fig. 5.2(a) that the pure-plunge case exhibits a slightly larger aerodynamic lag than the pure-pitching case whereby the pure-pitch case demonstrates a larger peak-to-peak lift variation. This discrepancy between the two analogous motions has also been observed by Soltani et al (2008) at higher Reynolds numbers and can be attributed to the relative positioning of the shed vortices. When examining the moment distribution in Fig. 5.2(b), the pure-pitching case demonstrates a much earlier recovery from moment stall, albeit with a strong overshoot into the pitch-up moment regime. This earlier recovery corresponds to the relative positioning of the shed LEV when compared to the pure-plunge case.

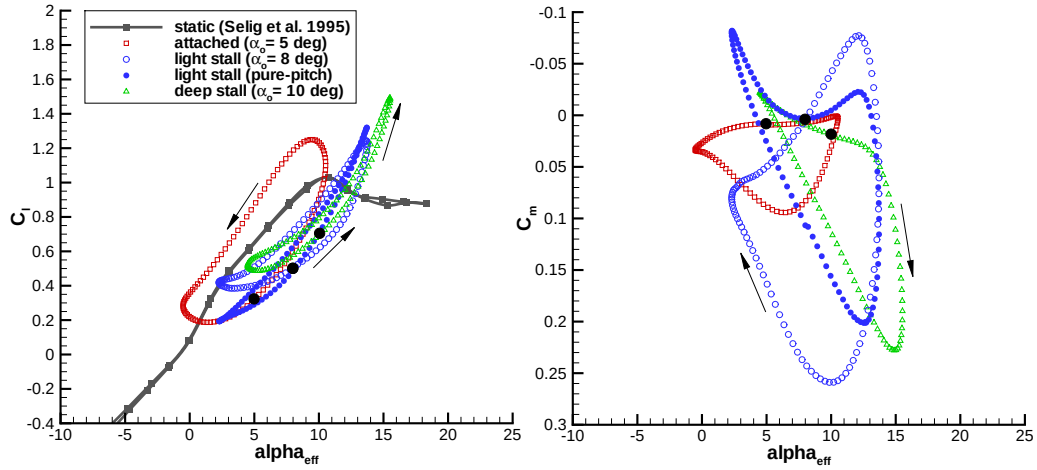

(a) lift hysteresis ($k = 0.1$) (b) moment hysteresis ($k = 0.1$)

Figure 5.2: Direct lift and moment coefficients for three pure-plunge cases ($\alpha_o = 5°, 8°$ and $10°$) and one equivalent pure-pitch case ($\alpha_o = 8°$) at $k = 0.1$; note black circle represents top of stroke.

In Fig. 5.4, comparisons of the pure-plunge and pure-pitch vortical wakes were found to be qualitatively very similar. For the bluff-body-type case ($k = 0.1$) shown in Fig. 5.4(a), it can be seen that only at $t/T = 2/16$ does a separation bubble first appear, whereby more pronounced for the pure-plunge case. In subsequent frames the pure-plunge case tends to develop more quickly than the pure-pitch case, both in the streamwise and in the normal directions. The broader development of the wake in the normal direction is due to the quick downwards movement of the airfoil in relation to the shed vortices. Thus in general a pure-pitch motion can be expected to have a more compact wake. For the mushroom-type case ($k = 0.25$), again the first appearance of a separation bubble can be found at $t/T = 2/16$. From then on the pure-plunging and pure-pitching cases share a nearly identical appearance.

Vortex Trajectories and Convective Velocities

PIV measurements for the pure-plunging and pure-pitching cases at $k = 0.25$ were performed to more accurately determine the vortex trajectories and their corresponding velocities in the wake.

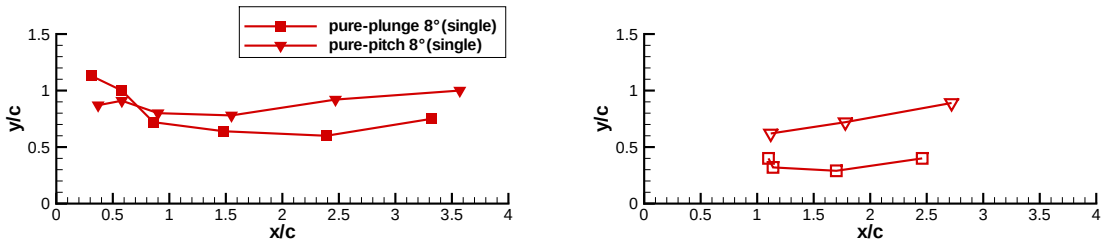

(a) LEV position (b) TEV position

Figure 5.3: Trajectories of LEV and TEV cores for the single-airfoil reference cases at $k = 0.25$.

(a) plunge ($k = 0.1$) (b) pitch ($k = 0.1$) (c) plunge ($k = 0.25$) (d) pitch ($k = 0.25$)

Figure 5.4: Comparison of equivalent pure-plunge and pure-pitch kinematics using smoke visualization with a mean angle of attack of $\alpha_o = 8°$; note sequences start at $t/T = 0$ (top of stroke) and follow in constant steps of $t/T = 1/16$.

Fig. 5.3(a) shows the LEV trajectories for the pure-plunging and pure-pitching motions. One can see that for pure-plunge that the LEV passes on a lower trajectory than for pure-pitch due to the large vertical displacement of the profile in the vertical direction. The LEV begins to develop at around timestep $t/T = 0.167$ and then stays over the airfoil surface during the plunge motion until it finally sheds at the end of the downstroke (see Fig. 6.6). In contrast, the pure-pitching airfoil always stays at the center position of the tunnel (trailing-edge excursion is small) and thus the wake is found to be narrower. Fig. 5.3(b) shows a similar offset in the TEV trajectories for the two cases.

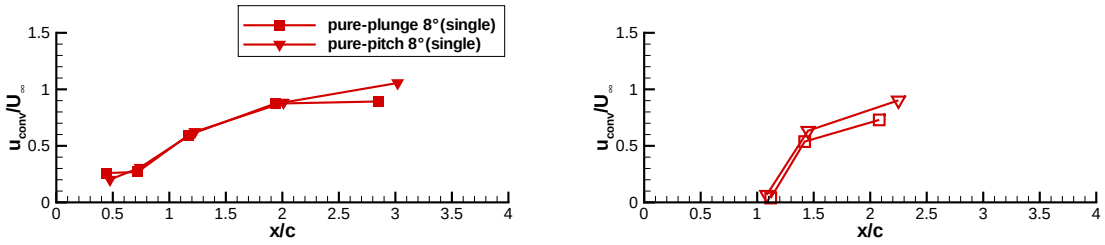

(a) LEV convection velocity

(b) TEV convection velocity

Figure 5.5: Convective velocities of LEV and TEV cores for the single airfoil reference cases at $k = 0.25$.

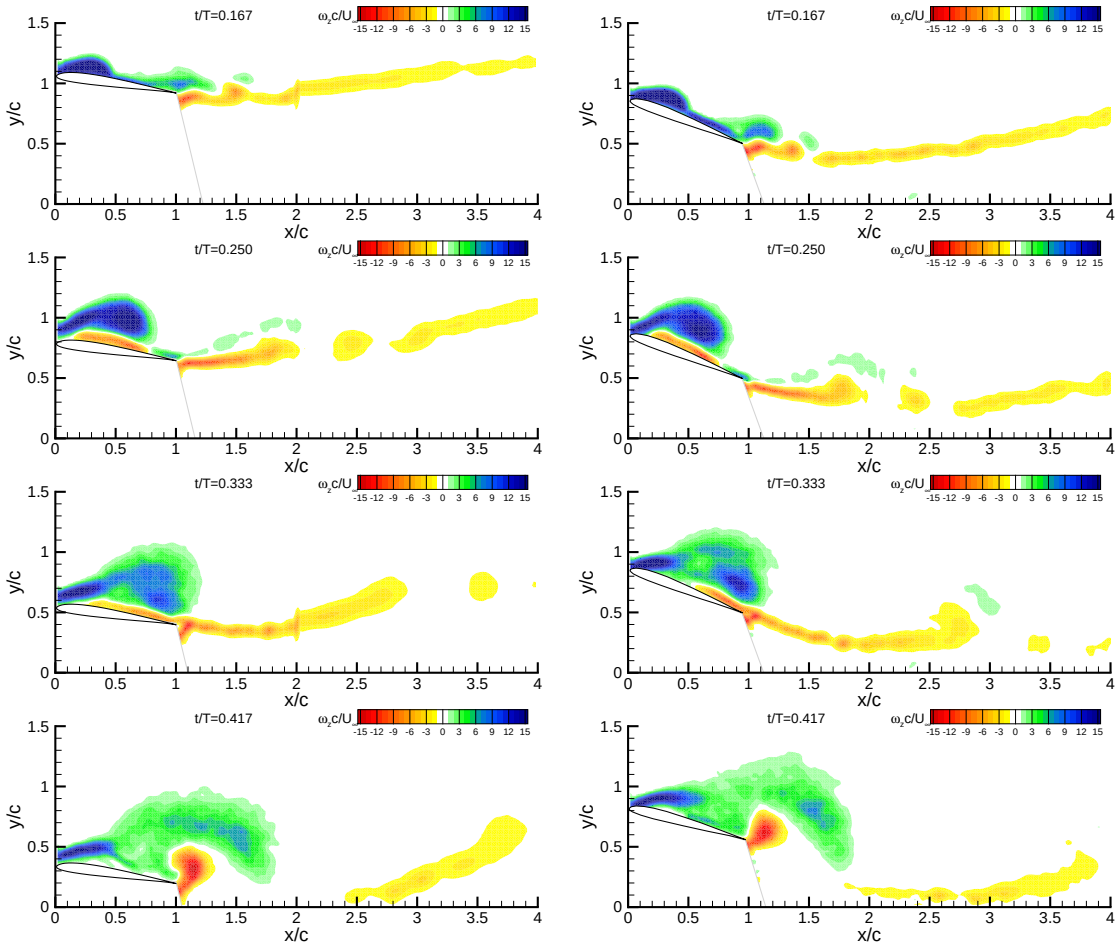

(a) pure-plunge

(b) pure-pitch

Figure 5.6: Plots of dimensionless vorticity for the pure-plunge reference case (a) and the pure-pitch case (b) at $k = 0.25$.

Fig. 5.5 shows the convection velocities of the LEVs and TEVs for a single airfoil performing pure-plunge and pure-pitch. The velocity development for pure-pitch and pure-plunge is nearly identical. In Fig. 5.5(a) one can see that it takes approximately two chord lengths for the LEV to reach free-stream velocity. Fig. 5.5(b) shows that the TEV accelerates more quickly than the LEV. The TEV reaches free-stream velocity within approximately one chord length from the trailing edge. When examining Fig. 6.6, it is clear that the overall development of the LEV and TEV is nearly identical for both kinematics. Again, the only variation is the relative height of the vortices, which can be attributed to the positioning of the airfoil itself.

5.2.3 Combined Motion

Direct force measurements for a combined pitching and plunging airfoil were performed as a means of examining the sensitivity of the main parameters such as reduced frequency (k), mean angle of attack (α_o) and amplitude of angle of attack (α_1), as well as to better understand the lift-augmentation available through dynamic stall. A range of combined pitch and plunge motions were examined for two reduced frequencies, i.e. $k = 0.05$ and 0.1. Already at these relatively low reduced frequencies strong hysteresis in both lift and moment coefficients were revealed. In both Figs. 5.7 and 5.8, with respective mean angles of attack of $\alpha_o = 5^\circ$ and $\alpha_o = 10^\circ$, the lift hysteresis curves change their sign of rotation from clockwise ($k = 0.05$) to counter-clockwise ($k = 0.1$). This is explained by the aerodynamic phase lag, which grows with increasing reduced frequency. This phenomenon is explained by the strong influence of the shed vortices in the wake on the bound airfoil circulation. Details of these unsteady (circulatory) effects are described in detail by Leishman (2006) in the context of rotorcraft aerodynamics.

From both Figs. 5.7(a) and 5.8(a), even at reduced frequencies as low as $k = 0.05$, clear signs of dynamic stall can be detected, observed as a strong lift overshoot beyond the peak static-stall lift value. This overshoot can be interpreted as an almost immediate adjustment of the pressure distribution to the incidence angle accompanied by a lag in stall credited to the slow viscous time scale of the boundary layer; hence the process is often referred to as *delayed stall*. A range of effective angle-of-attack variations and associated dynamic-stall regimes are plotted representing *attached*, *light-stall*, *deep-stall* and *very deep-stall* cases following the nomenclature of McCroskey (1982) on dynamic stall for pitching airfoils. These names refer to the level of separation encountered over the course of a given cycle. When examining the moment hysteresis curves, moment stall, as would be expected, is found to increase with deeper stall conditions (seen as a sharp drop from the neutral moment condition), which is clearly found when comparing Figs. 5.7(b) to 5.8(b) or Figs. 5.7(d) to 5.8(d) with one another. This strong moment stall can be explained by the convection of the LEV along the airfoil surface. Once this low-pressure vortical structure passes the quarter-chord position, a strong pitch-down moment is generated until it sheds from the trailing edge, at which point the moment returns back to the neutral position. It can be seen for all cases that moment stall always occurs before lift stall. This is due to the fact that moment stall occurs as soon as the LEV moves aft of the point of rotation whereas lift stall only occurs once the vortices are completely shed from the trailing edge.

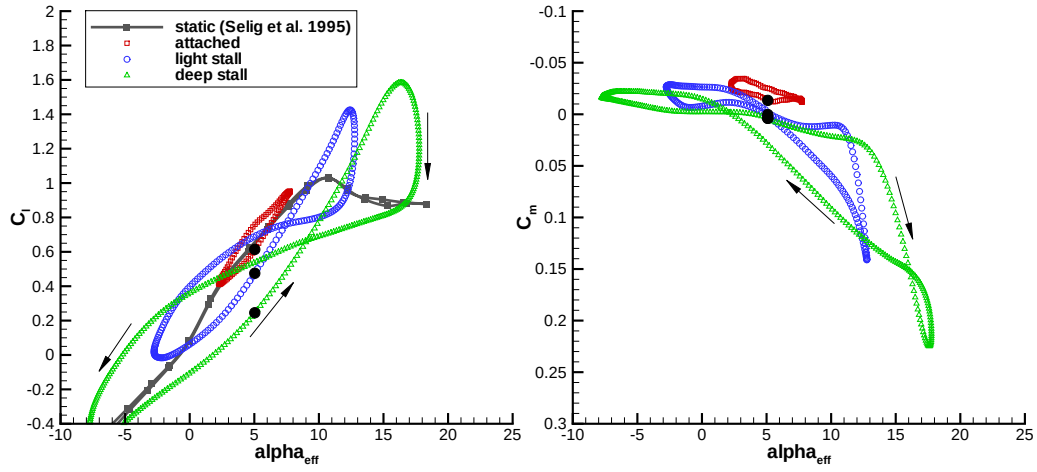

(a) lift hysteresis ($k = 0.05$) (b) moment hysteresis ($k = 0.05$)

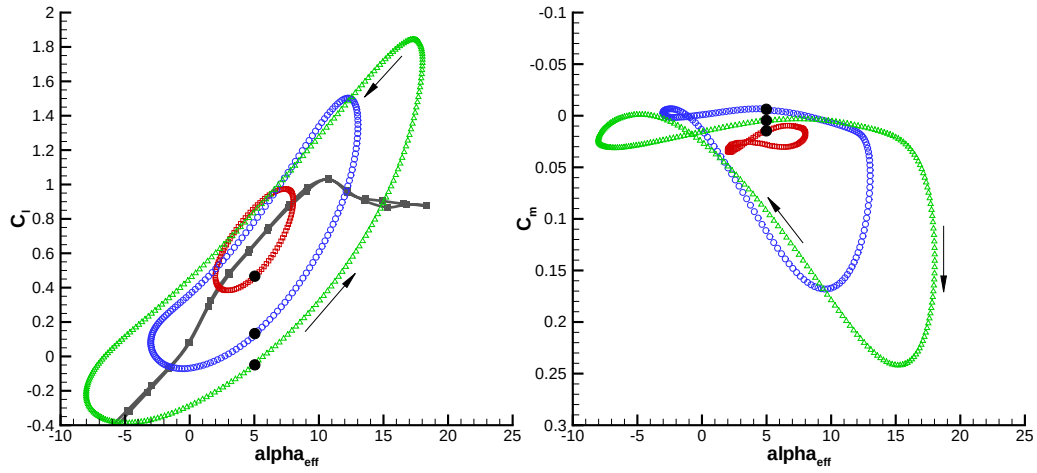

(c) lift hysteresis ($k = 0.1$) (d) moment hysteresis ($k = 0.1$)

Figure 5.7: Direct lift and moment coefficients for three effective angle-of-attack variations and a mean angle of attack of $\alpha_o = 5°$; note black circle represents top of stroke.

When examining in more detail the moment hysteresis curves in Fig. 5.7, the ever-stronger nose-down pitching moment is explained by the growing strength of the LEVs from light-stall to deep-stall, and even to very deep-stall conditions. A further interesting feature to note is the difference in shape of the hysteresis curves between $k = 0.05$ and $k = 0.1$. In Fig. 5.7(c) counterclockwise lift loops are found, suggesting a much larger aerodynamic phase lag than for the lower reduced frequency of $k = 0.05$. This can be explained by the extra relative dwell time of the LEVs over the airfoil surface for the higher reduced-frequency cases. Moving on to the deeper stall cases in Fig. 5.8 with $\alpha_o = 10°$, one finds, as would be expected, an earlier stall during the downstroke (Fig. 5.8(a)) and even larger nose-down aerodynamic moments (Fig. 5.8(b)). At the higher reduced frequency of $k = 0.1$ peak lift is generated at the bottom of the stroke, representative of an aerodynamic phase lag of nearly $t/T = 0.25$. The corresponding nose-down moments in Fig. 5.8(d) recover later in the upstroke when compared to the lower reduced frequency case in Fig. 5.8(b). Despite the increase in hysteresis found for this higher mean angle of attack, peak lift is only marginally changed when compared to the deep-stall case in Fig. 5.7(c).

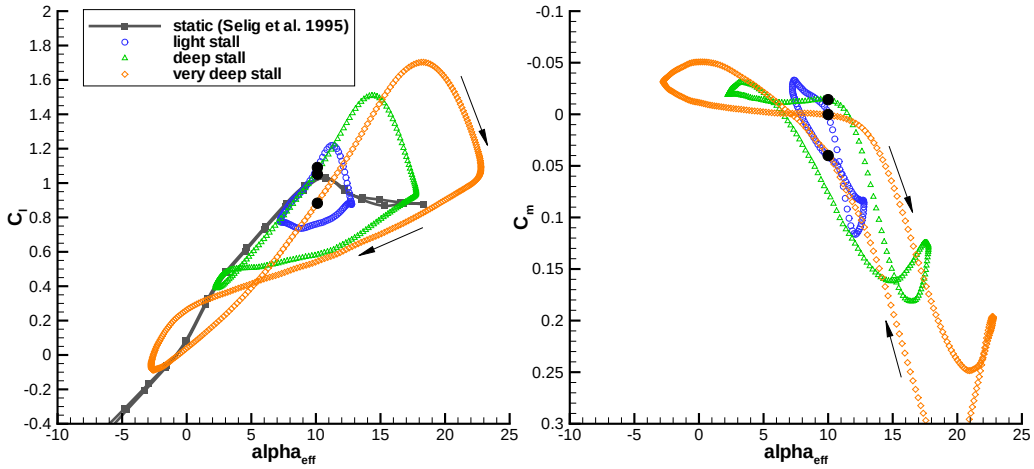

(a) lift hysteresis ($k = 0.05$) (b) moment hysteresis ($k = 0.05$)

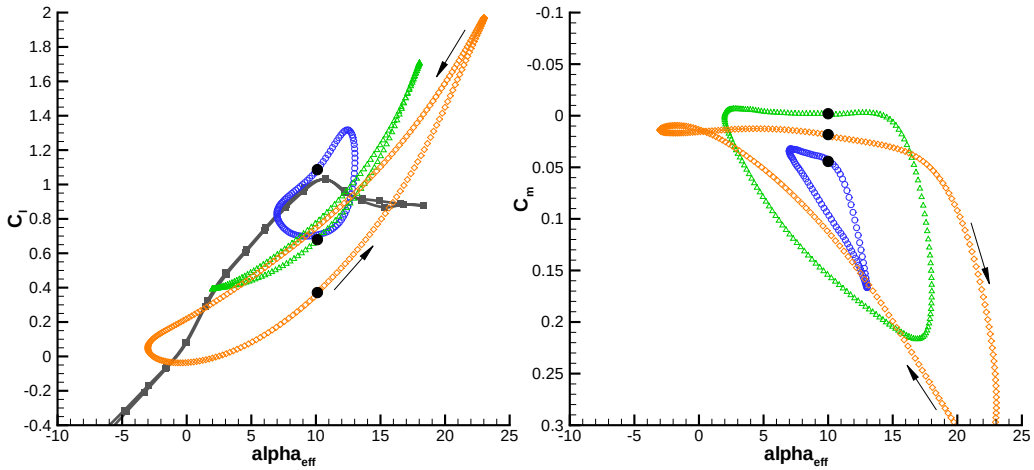

(c) lift hysteresis ($k = 0.1$) (d) moment hysteresis ($k = 0.1$)

Figure 5.8: Direct lift and moment coefficients for three effective angle-of-attack variations and a mean angle of attack of $\alpha_o = 10°$; note black circle represents top of stroke.

A final comparison of the peak lift and moment coefficients for all combined cases is made in Fig. 5.9. Here it is found that the deep-stall case from Fig. 5.7(c), with a reduced frequency of $k = 0.1$, shows very strong lift augmentation combined with a relatively low pitch-down moment. For the higher mean angle of attack of $\alpha_o = 10°$ there is a marginal improvement in lift but at the price of a larger peak pitch-down moment. This suggests that lift augmentation in the light-stall to deep-stall regimes is most effective, particularly at higher reduced frequencies.

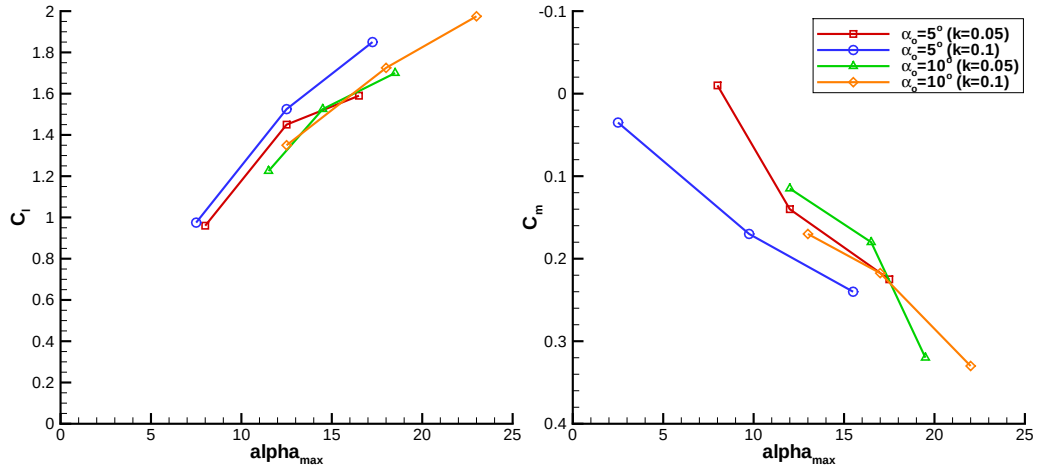

(a) peak lift (b) peak moment

Figure 5.9: Maximum lift and moment coefficients taken from Figs. 5.7 and 5.8.

5.3 Summary

The effect of reduced frequency and angle of attack (both mean and amplitude) have been investigated for decomposed and combined pitching and plunging cases. A clear transition from a bluff-body-type to a mushroom-type wake is apparent at a reduced frequency of approximately $k = 0.2$. A comparison of pure-plunging and pure-pitching cases suggests that the equivalent flow fields are nearly identical and that variations in lift and moment are only a function of the shed vortex positioning relative to the airfoil itself. For the combined pitch/plunge cases, the mean angle of attack (α_o) was found to be an important parameter since it dictated to a large extent the level of dynamic stall found over the profile. When increasing from $k = 0.05$ to $k = 0.1$, the hysteresis curves were observed to switch from the clockwise to the counter-clockwise directions, representing an increase in the total aerodynamic lag of approximately $t/T = 0.125$. Progressive increases in lift were achieved by moving from the stall-onset, to light-stall and finally to the deep-stall regime. A slightly greater augmentation in lift (and aerodynamic lag) was generally found for the higher reduced-frequency cases ($k = 0.1$). However, when operating at deep-stall or beyond, large nose-down pitching moments (or moment stall) could not be avoided.